

1 Natural Marine Cloud Brightening in the Southern Ocean

2

3 Gerald G. Mace¹, Sally Benson¹, Ruhi Humphries^{2,3}, Peter M. Gombert¹, Elizabeth
4 Sterner¹

5

6 ¹Department of Atmospheric Sciences, University of Utah, Salt Lake City, Utah

7 ²Climate Science Centre, CSIRO Oceans and Atmosphere, Melbourne, Australia

8 ³Australian Antarctic Program Partnership, Institute for Marine and Antarctic Studies,
9 University of Tasmania, Hobart, Tasmania, Australia

10

11 Corresponding Author Information:

12 Gerald "Jay" Mace, Professor

13 Department of Atmospheric Sciences, University of Utah

14 135 South 1460 East Rm 819 (819 WBB)

15 Salt Lake City, Utah, 84112-0110

16 Cell Phone: 801 201 7944

17 Office Phone: 801 585 9489

18 Email: jay.mace@utah.edu

19 Fax: 801 860 0381

20

21

22

23 Abstract: The number of cloud droplets per unit volume (N_d) is a fundamentally
24 important property of marine boundary layer (MBL) liquid clouds that, at constant liquid
25 water path, exerts considerable controls on albedo. Past work has shown that regional
26 N_d has direct correlation to marine primary productivity (PP) because of the role of
27 seasonally varying biogenically-derived precursor gasses in modulating secondary
28 aerosol properties. These linkages are thought to be observable over the high latitude
29 oceans where strong seasonal variability in aerosol and meteorology covary in mostly
30 pristine environments. Here, we examine N_d variability derived from five years of MODIS
31 level-2 derived cloud properties in a broad region of the summer Eastern Southern Ocean
32 and adjacent marginal seas. We demonstrate latitudinal, longitudinal, and temporal
33 gradients in N_d that are strongly correlated with the passage of air masses over high PP
34 waters that are mostly concentrated along the Antarctic Shelf poleward of 60°S. We find
35 that the albedo of MBL clouds in the latitudes south of 60°S is significantly higher than
36 similar LWP clouds north of this latitude.

37
38 Short Summary: The number cloud droplets per unit volume is a significantly
39 important property of clouds that controls their reflective properties. Computer models of
40 the Earth's atmosphere and climate have low skill at predicting the reflective properties of
41 Southern Ocean clouds. Here we investigate the properties of those clouds using satellite
42 data and find that the cloud droplet number in the Southern Ocean is related to the
43 oceanic phytoplankton abundance near Antarctica and cause clouds there to be
44 significantly brighter than clouds further north.

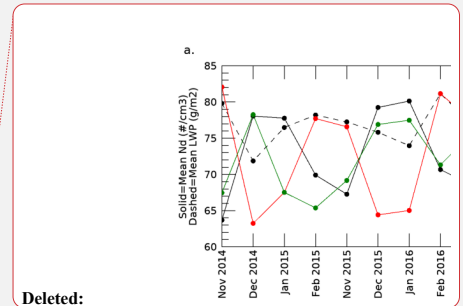
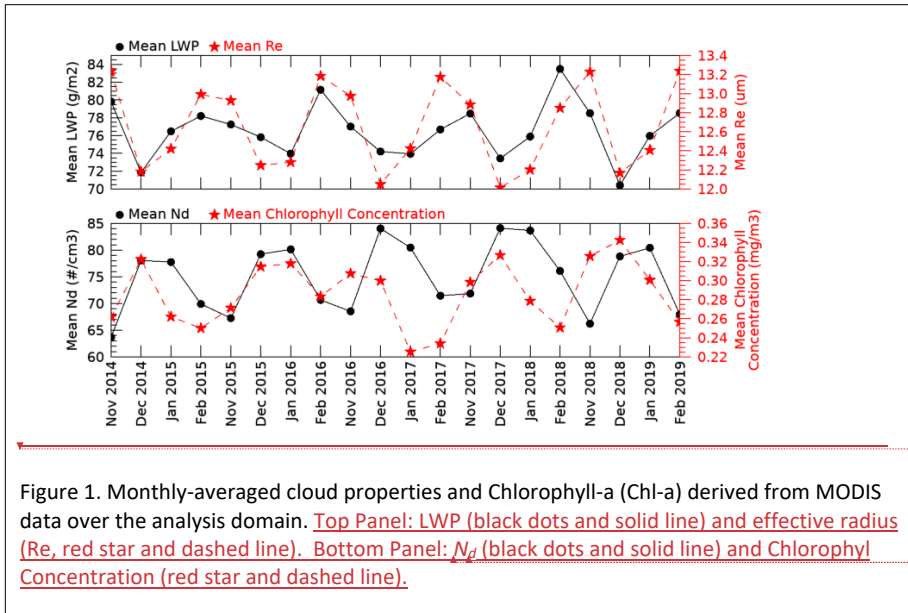
45 1. Introduction

46
47 The cloud and precipitation properties of the Southern Ocean (SO) have received
48 considerable attention since Trenberth and Fasullo (2010) identified a high bias in
49 surface-absorbed solar energy there (McFarquhar et al., 2020). This bias has been
50 traced to erroneously small Marine Boundary Layer (MBL) cloud cover in simulations of
51 the Southern Ocean climate (Bodas-Salcedo, et al., 2016; Naud et al., 2016). The
52 actual SO cloud climatology and associated albedo are dominated by geometrically thin
53 MBL clouds (Mace et al., 2010; Mace et al., 2020, 2021). Because the predominant
54 shallow boundary layer clouds rarely precipitate (Huang et al., 2016), they are sensitive
55 to cloud condensation nuclei (CCN) concentrations (Twohy and Anderson, 2008;
56 Painemal et al., 2017).

Deleted: ; Petters and Kreidenweis, 2007

57
58 In the SO, the CCN seasonal cycle (Ayers and Gras, 1991; Vallina et al. 2006; Gras and
59 Keywood, 2017) is reflected in basin-wide cloud property variations (Krüger and Graßl,
60 2011). McCoy et al. (2015) and Mace and Avey (2017) also found that MODIS- and A-
61 Train-derived cloud properties over the SO, demonstrate a similar seasonal cycle in
62 cloud droplet number concentration (N_d) as for CCN. The basin wide variability in CCN
63 and cloud albedo have been shown to be correlated with marine primary productivity
64 (PP – defined as the net organic matter, mostly produced by phytoplankton, that is
65 suspended in the ocean; Vallina et al., 2006; Krüger and Graßl, 2011; McCoy et al.,
66 2015). McCoy et al. (2020) argue that the SO can be viewed as an analog of the
67 preindustrial Earth. Given the large natural seasonal variability in CCN and clouds, the
68

70 SO is a natural laboratory to understand the processes that contribute to simulated
 71 aerosol-related indirect forcing variability in climate models (Carslaw et al. 2013).
 72
 73 CCN and cloud droplet N_d in the SO are higher in Summer when significant latitudinal
 74 gradients have been documented in the SO Australasian sector (Humphries et al.,
 75 2021). Using time of flight aerosol chemical speciation monitor (ACSM) and ion



Deleted:

Formatted: Font: Italic

Formatted: Font: Italic, Subscript

76 concentrations from filter samples, Humphries et al., (2021) analyzed the covariance of
 77 aerosol chemistry, CCN at 0.5% supersaturation, and Condensation Nuclei (CN) larger
 78 than 10 nm collected aboard Australian research vessels during the 2018 Austral
 79 Summer (McFarquhar et al., 2021). While sulfates were a major compositional
 80 component of aerosol at all latitudes during summer these compounds were in higher
 81 fractional abundance poleward of 65°S where overall CCN numbers were higher by
 82 ~50%. Chloride derived from sea salt was dominant in the region equatorward of 65°S
 83 but was mostly absent south of 65°S. The ratio of CCN to CN at 0.5% supersaturation
 84 increased considerably south of 65°S suggesting unique aerosol chemical processes,
 85 compared to the open ocean. Humphries et al. (2021) also discusses how this
 86 compositional boundary in aerosol chemistry is often very distinct in the East Antarctic
 87 waters between 60°S and 65°S. Following Humphries et al. we will refer to this belt as
 88 the Atmosphere Compositional Front of Antarctica (ACFA). Humphries et al. (2021)
 89 conclude that aerosol, newly condensed from gas phase sulfur species such as from
 90 the oxidation of dimethyl sulfide (DMS), are an important component of high latitude
 91 CCN. These products of phytoplankton physiology are released into the atmosphere

Deleted: stry

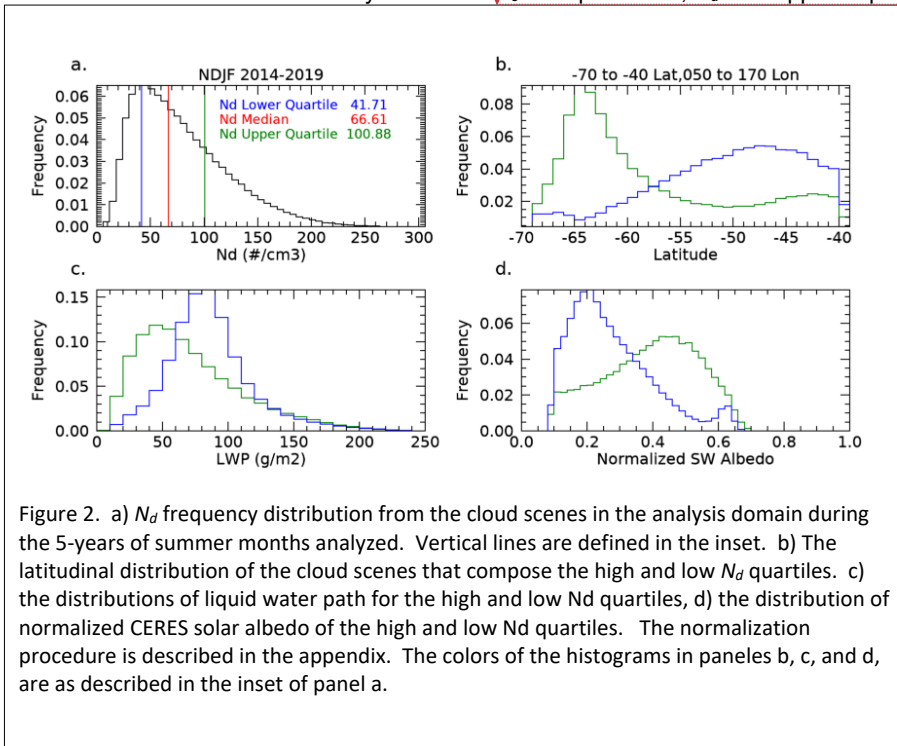
93 from the highly productive waters from ~60°S to the Antarctic – a region well known for
94 a vast marine food web (Deppler and Davidson, 2017; Behrenfeld et al., 2016).
95
96 Mace et al. (2021a) derived N_d and other cloud microphysical properties from non-
97 precipitating stratocumulus clouds using shipborne remote sensing data. They found
98 that stratiform clouds poleward of the ACFA had significantly higher N_d than
99 equatorward. One particular case took place when the Icebreaker Aurora Australis was
100 at the Davis Antarctic station just east of Prydz Bay (~77°E) between 1 and 5 January
101 2018 and featured nearly continuous high N_d clouds ($> 150 \text{ cm}^{-3}$) occurring in a
102 southerly flow passing over the ship that had trajectories from the Antarctic Continent.
103 Similarly, Twohy et al., (2021) report that the highest concentrations of aerosol
104 composed primarily of non-sea salt sulfates in the free troposphere north of 60°S
105 observed from research aircraft in Summer 2018 had occurred in airmasses that had
106 originated recently from over the Antarctic continent. See also Shaw et al. (1988) for an
107 early examination of the role of biogenic sulfate in modulating summertime aerosol
108 along coastal Antarctica. Shaw et al. (2007) expands on this idea as does Korhonen et
109 al., (2008).

Formatted: Font: Italic
Formatted: Font: Italic, Subscript
Deleted: sulfur-based

110
111
112
113 2. Results
114

116 See Appendix A for methods and definitions. Approximately 40,000 1° latitude by 2°
 117 longitude MBL cloud scenes per month meet our criteria for liquid phase non
 118 precipitating clouds in the analysis domain. This number varies by ~25% in a seasonal
 119 cycle that is due mostly to our solar zenith angle criteria. A seasonal cycle is evident in
 120 the monthly-averaged cloud properties. LWP and r_e have seasonal minima in the
 121 months of December and January. Due to an $r_e^{-5/2}$ dependence, N_d is of opposite phase

Deleted:



122 with r_e and correlated with it at -0.93. The seasonal variability in LWP (r_e) is on the
 123 order of 7% (4%) and is small in comparison to N_d (~25%). τ and r_e are derived from
 124 the visible and near infrared reflectances with the MODIS level 2 retrieval algorithm
 125 (Nakajima and King, 1990). LWP is, then, derived from

$$\tau = \frac{3}{2\rho_w} \frac{LWP}{r_e} \quad \text{Equation 1.}$$

Deleted: a relationship like

128 that is derived in Stephens (1978). It is reasonable to consider whether seasonal
 129 variations in N_d , perhaps linked to CCN, might be associated with variability in LWP.
 130 We find that LWP decreases as N_d increases with a correlation coefficient in the
 131 monthly means of -0.60 in the monthly means.

Formatted: Right

Deleted: (

Deleted: ,

Deleted: of Figure 1

139 In four of the five years, we see by inspection of Figure 1 that Chl-a leads changes in N_d
140 by approximately 1 month. The correlation coefficient of N_d and Chl-a increases from
141 0.27 to 0.60 when N_d is lagged from 0 to 1 month in the Figure 1 time series although
142 this result should be interpreted with caution given the break between February and
143 November in the time series. These results are broadly like those presented by McCoy
144 et al., (2015) and Mace and Avey (2017). McCoy et al. (2015) link N_d variations to PP
145 using regression analysis of MODIS derived N_d against a biogeochemical
146 parameterization of biogenic sulfate and organic mass fraction (See also Lana et al.,
147 2012).

148
149 We find a broad distribution of scene-averaged N_d (Figure 2a) with median, lower and
150 upper quartile values of 66 cm^{-3} , 42 cm^{-3} and 101 cm^{-3} respectively. Henceforth, we
151 focus our analysis on the groups of scenes that are less than and greater than the
152 upper and lower quartiles. The high and low N_d scenes have distinct latitudinal
153 occurrence distributions (Figure 2b) with low N_d scenes peaking broadly at 48°S while
154 the high N_d scenes demonstrate a modal occurrence near 64°S . Overall, the N_d gradient
155 implied by Figure 2 is correlated with the latitudinal distribution of imager-derived Chl-a
156 (i.e., Deppler and Davidson, 2017). The seasonally averaged N_d gradient is also
157 discussed in McCoy et al., (2020). Differentiating seasonally varying properties north
158 and south of the ACFA (not shown), we find a clear differentiation in r_e and N_d with
159 smaller r_e south of the ACFA (mean $r_e \sim 11 \mu\text{m}$, $N_d \sim 100$) compared to north (mean
160 $r_e \sim 13 \mu\text{m}$, $N_d \sim 67 \text{ cm}^{-3}$). LWP is slightly larger by $\sim 7\%$ south of the ACFA. Both
161 regions have a distinct seasonal cycle in cloud properties shown in Figure 1 although
162 the southern latitudes have larger interannual variability likely owing to variations in
163 annual sea ice extent and melt. The LWP distribution of the high N_d quartile is
164 significantly shifted to lower values compared to the low N_d quartile LWP distribution
165 (Figure 2c). This finding is in accordance with the observational and theoretical work
166 presented in Glassmeier et al., (2021) who argue that closed cell stratocumulus that
167 dominate the clouds examined here have increased entrainment drying under higher N_d
168 conditions. Figure 2c and 2d illustrate that even though the high N_d quartile scenes tend
169 to have lower LWP, their solar albedo (A) tends to be significantly higher than the low
170 N_d quartile scenes illustrating the influence of cloud microphysics on the radiative
171 forcing of these clouds.

172
173 The high N_d scenes occur predominantly poleward of the ACFA (Figure 3). Interestingly
174 we find that the latitudinal gradient weakens slightly west of 90°E with a broad region of
175 higher N_d occurrence in the vicinity of the Kerguelen Rise where PP is higher (Cavagna
176 et al., 2015). Establishing causality between regions of high PP and cloud properties is
177 challenging (i.e., Meskhidze and Nenes, 2006; Miller and Yuter, 2008). While we find
178 seasonal associations over broad regions here, the chain of causality between
179 phytoplankton and clouds is not immediate or even necessarily direct because the
180 chemical processes take time to evolve and can move along chemical pathways that
181 have divergent outcomes (Woodhouse et al., 2013). To increase cloud N_d , new CCN
182 must be formed. Formation of new CCN can occur when sulfur compounds emitted
183 from the ocean surface nucleate after oxidation in the presence of sunlight. This
184 process of new particle formation occurs in the absence of other aerosol and often

185 requires mixing of the gaseous compounds from the boundary layer into the low-aerosol
186 free-troposphere where the newly formed aerosol can be transported widely (Shaw,
187 2007; Korhonen et al., 2008). Other pathways are possible such as deposition of
188 sulfate compounds onto primary sea salt particles that modify the chemical properties of
189 existing CCN rather than nucleating new CCN (Fossum et al., 2020) or even removal of
190 sulfur compounds from the gas phase via aqueous phase oxidation in clouds
191 (Woodhouse et al., 2013).
192

Deleted: chemical

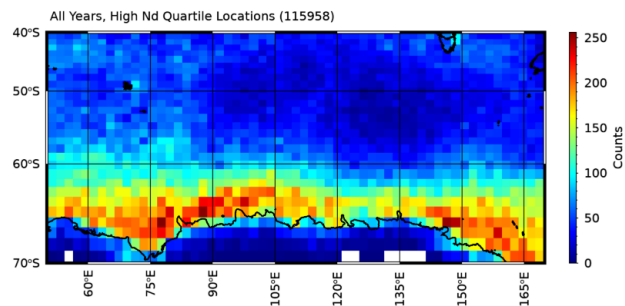


Figure 3. Geographic distribution of the high N_d quartile cloud scenes. Number in parentheses show the total of number cloud scenes from the 5-year summer data set.

193 Given the foregoing discussion, it seems reasonable that an air mass that is producing
194 clouds with certain features could be interacting with an aerosol population that has
195 evolved over periods of days (Brechtel et al., 1998). In addition, natural cloud
196 processes such as collision and coalescence of drops tend to cause N_d to decrease
197 while precipitation efficiently scavenges CCN, thereby lowering CCN concentration and
198 even modifying their composition and size through aqueous processing (Hoppel et al.,
199 1986). With larger r_e north of the ACFA, the collision-coalescence process is likely more
200 active (Freud and Rosenfeld, 2012) and could explain the latitudinal difference in
201 adiabaticity (see methods) found in in situ data. For instance, Kang et al. (2022)
202 analyzed data collected from Macquarie Island (54.6°S, 158.9°E) and found that, not
203 only were most clouds drizzling, but that precipitation as light as 0.01 mm hr⁻¹ could
204 reduce N_d by ~50%. Therefore, a cloud field should be considered as the product of
205 both local dynamics and thermodynamics primarily with modulation by a local
206 population of CCN. To examine the role of air mass history, we calculate the 5-day back
207 trajectories using the Hybrid Single-Particle Lagrangian Integrated Trajectory (HYSPLIT;
208 Stein et al., 2015) model using the Global Data Assimilation System (GDAS; Kamitsu,
209 1989) as input. The parcel's endpoint is the central latitude and longitude of the cloud
210 scene, and the location and model output are stored hourly.
211

213 South of the ACFA, the histories of the populations tend to be statistically different
214 (Figure 4). The low N_d clouds are more likely to be observed in airmasses that have
215 trajectories that originated in the open ocean region to the north of the ACFA. High N_d
216 scenes rarely evolve in airmasses that originate in the open ocean to the north of the
217 ACFA. The likelihood is that an airmass that has produced a high N_d cloud scene south
218 of the ACFA latitude has spent most of the previous 5 days over latitudes south of the
219 ACFA. North of the ACFA, the latitude distributions during the months of November and
220 February (not shown) are essentially identical for the high and low N_d quartiles.
221 However, for December and January, we find that the high N_d clouds observed north of
222 the ACFA have an increased likelihood of trajectories emanating from south of the
223 ACFA during the 5-days prior to the MODIS observation.

224

225 3. Discussion and Conclusions

226

227 Using MODIS level 2 cloud property retrievals and the technique developed in
228 Grosvenor et al. (2018; hereafter G18) to estimate N_d , we examine the latitudinal and
229 seasonal cycles of non-precipitating liquid-phase clouds in the Australasian sector of the
230 Summertime Southern Ocean. The r_e and N_d have distinctive differences north and
231 south of the ACFA but demonstrate similar seasonal cycles. We infer that the spatial
232 and temporal variability in cloud N_d , and r_e are at least partially a function of the
233 geographic and temporal variability in CCN that, in turn, is related to the seasonality of
234 primary sources such as sea salt and the latitudinal variability in marine PP. The
235 highest N_d clouds tend to be overwhelmingly found along the East Antarctic coastal
236 waters south of the ACFA.

237

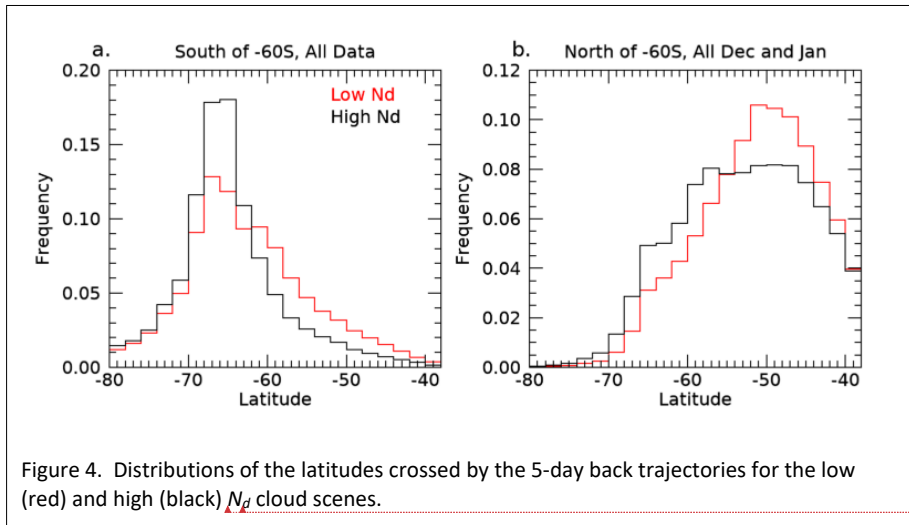


Figure 4. Distributions of the latitudes crossed by the 5-day back trajectories for the low (red) and high (black) N_d cloud scenes.

Formatted: Font: Italic
Formatted: Font: Italic, Subscript

238 Because aerosol precursor gasses like DMS often require trajectories through the free
 239 troposphere to nucleate new particles that then take time to reach CCN sizes
 240 (Korohonen et al., 2008; Shaw et al. 2007), we examine the back trajectories of the
 241 air masses observed with high and low N_d south of the ACFA and find significant
 242 differences. Low N_d cloud scenes are more likely to have arrived south of the ACFA
 243 from northerly trajectories that would have transported low CCN air dominated by sea
 244 salt. The high N_d cloud scenes are more likely to have trajectories that have remained
 245 adjacent to or had passed over the Antarctic continent. North of the ACFA, while the
 246 trajectory statistics for the high and low N_d quartiles in November and February are
 247 nearly identical, during December and January the high N_d clouds scenes tend to have
 248 an increased likelihood of arriving north of the ACFA from southerly trajectories,
 249 suggesting that high CCN air masses are being transported northward especially during
 250 December and January.

251
 252 Given that the main difference between the source regions north and south of the ACFA
 253 is the magnitude of the marine PP, and given previous analyses of CCN compositional
 254 sensitivity to marine biological factors (e.g. Humphries et al., 2021; Vallina et al., 2006;
 255 Lana et al., 2012; McCoy et al., 2015), we conclude that the biological source of sulfate
 256 precursor gasses and the slackening of surface winds with latitude during Summer
 257 plays a dominating role in controlling the latitudinal gradients in the properties of weakly
 258 precipitating MBL cloud fields over the Southern Ocean. Figure 5 summarizes our
 259 findings by presenting composite seasonal cycles of MBL cloud scenes north and south
 260 of 60°S. The LWP in both latitudinal bands go through a weak seasonal cycle. The
 261 significant contrast in optical depth between the northern and southern bands is, we
 262 infer, mostly caused by the latitudinal contrast in N_d . Based on available evidence, we
 263 conclude that the differences in r_e in MODIS retrievals are causally linked to oceanic PP

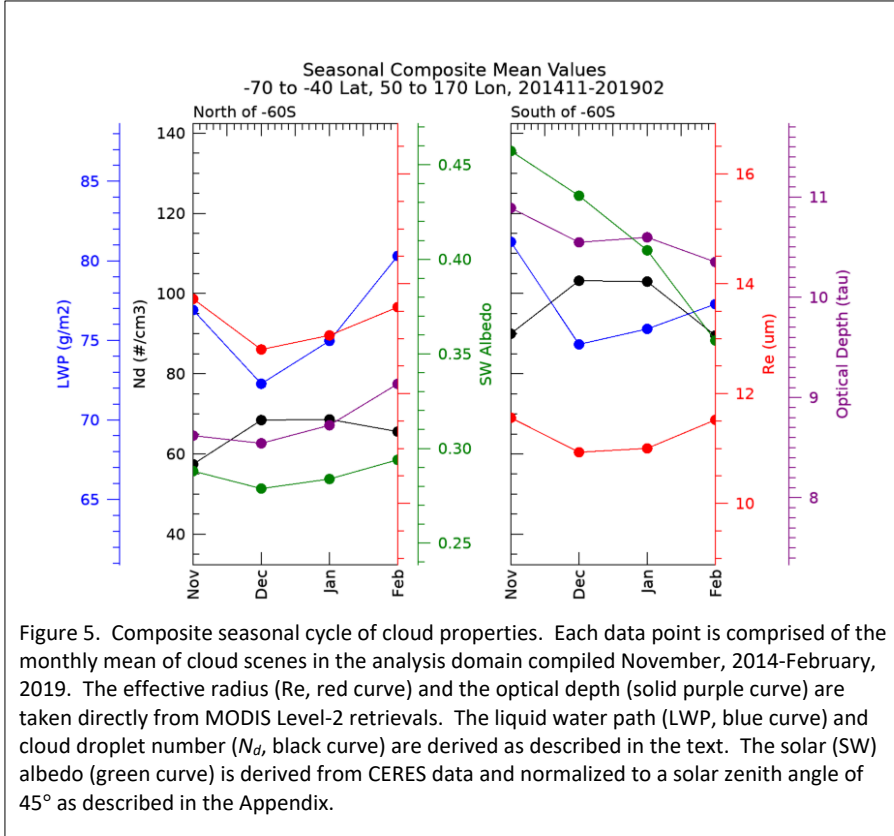
264 gradients that drive CCN, and thereby N_d , to be higher over the southern region. This
265 sensitivity, in turn, plays a significant role in modulating the regional albedo (A) and,
266 thereby, influences the input of sunlight to the surface ocean. We note that the
267 seasonal cycle in A is different between the northern and southern latitude domains (a
268 topic for future work), however, always A of the southern domain is higher than that of
269 the northern domain. However, we should be careful not to overstate this case. Cloud
270 processes that consume N_d and modify CCN (i.e. precipitation and cloud processing)
271 also play a role in modulating cloud N_d and therefore regional A (Kang et al., 2022;
272 McCoy et al., 2020). The airmass history and source region, while apparently
273 important, are among many factors involved.

274

275 Since the magnitude of PP is significantly lower north of the ACFA throughout the
276 summer season, a similar seasonal cycle in N_d and r_e suggests that CCN derived from
277 DMS oxidation of precursor gasses emitted primarily from Antarctic coastal waters
278 perhaps seeds much of the rest of the Southern Ocean with biogenic sulfate aerosol as
279 observed in recent airborne observations (Twohy et al., 2021). The northerly transport
280 of these high sulfate airmasses out of the Antarctic coastal waters (Figure 4b) and
281 southerly transport of low sulfate air masses into the Antarctic coastal region near the
282 surface (Figure 4a) have been reported by Humphries et al. (2016, 2021) and Shaw
283 (1988) and observed in the free troposphere with recent research aircraft
284 measurements (Twohy et al. 2021).

285

286 Our ability to identify natural marine cloud brightening (Latham et al., 2008) due to
287 aerosol-cloud coupling is a direct result of the absence of other anthropogenic and
288 continental influences in the pristine SO. As argued by McCoy et al. (2020), it seems
289 clear that in several important ways, the Southern Ocean is the last vestige of the
290 preindustrial atmosphere allowing us to constrain processes that remain important to
291 our understanding of the global climate (Carslaw et al., 2013).



293 Appendix. Methods

294

295 We use MODIS imager-derived Level-2 retrievals (Platnick et al., 2015) of effective
 296 radius (r_e) and optical depth (τ) from five summer periods (2014-2019) collected
 297 between the latitudes of 45°S and 76°S and longitudes of 40°E and 170°E to focus
 298 roughly on where the ships and aircraft sampled in Summer 2017-18. We calculate N_d
 299 using the method derived and evaluated in G18:

300

$$301 \quad N_d = \frac{\sqrt{5}}{2\pi\kappa} \left(\frac{f_{ad}c_w\tau}{Q_{ext}\rho_w r_e^5} \right)^{1/2} \quad (\text{A1})$$

302

303 where ρ_w is the density of liquid water (1 g cm^{-3}), f_{ad} is an adiabaticity assumption, c_w is
 304 the vertical derivative of the adiabatic liquid water content, Q_{ext} is the extinction efficiency
 305 that is typically assumed to be 2 for cloud droplets, and κ is the cubed ratio of r_e to r_v . As

306 noted by G18, N_d depends on $r_e^{-5/2}$, which implies that the sensitivity or the rate of change
307 of N_d to retrieved r_e goes as the $-7/2$ exponent. Any biases in r_e , then would significantly
308 bias N_d . G18 provide a thorough evaluation of the sources of uncertainty in N_d due to
309 assumptions of adiabaticity, scene heterogeneity, etc., and conclude that N_d derived
310 using equation 1 applied to MODIS cloud retrievals has an overall uncertainty of $\sim 80\%$.

311
312 The most uncertain quantity in the assumptions used in Equation A1 is f_{ad} since the cloud
313 vertical structure is not constrained by MODIS measurements. Using cloud thickness from
314 ship-based cloud radar and lidar along with retrieved LWP from collocated microwave
315 radiometer (Mace et al., 2021a), we estimate the value of f_{ad} in nonprecipitating
316 stratocumulus observed during the summer of 2018 (McFarquhar et al., 2021). We find
317 that the mean and standard deviation of f_{ad} north of the ACFA is 0.66 and 0.48,
318 respectively. South of the ACFA, the mean and standard deviation of f_{ad} is 0.93 and 0.60,
319 respectively. For the calculations of N_d in equation A1, we use a constant value for f_{ad} of
320 0.8. N_d is proportional to the square root of f_{ad} , therefore, $\frac{\partial \ln N_d}{\partial \ln f_{ad}} = \frac{1}{2}$ and a fractional
321 variation in f_{ad} on the order of 0.5 would imply an uncertainty in N_d of 0.25. Furthermore,
322 we expect in regions with f_{ad} higher (lower) than 0.8 the N_d would be biased low (high).
323 As we show, the regions with higher N_d tend to be in the south and lower N_d in the north
324 counter to these expected biases. Additionally in this study, we will be examining
325 differences in spatially averaged N_d that are greater than a factor of 2. These results
326 imply that bias and random error due to uncertainty in f_{ad} is unlikely to significantly
327 influence the qualitative findings of this study.

328
329 Another source of systematic bias could be from the quantity κ that can be shown to be
330 a function of the variance of the droplet size distribution and is assumed to be a constant
331 at 0.7. G18 discusses this issue in some detail and concludes that there may be
332 systematic biases on the order of 12% that could be a function of N_d in pristine conditions.
333 While this quantity can be investigated with data collected in situ, no such data exists in
334 stratocumulus clouds south of the ACFA. Therefore, we recognize a potential source of
335 bias due to κ that is likely much smaller than the systematic latitudinal differences we find.

336
337 Given the uncertainties in N_d at the pixel level, we implement a filtering and averaging
338 scheme to focus on liquid phase, weakly precipitating cloud scenes. We define a scene
339 as a 1° latitude by 2° longitude domain where pixels are reported in the MODIS L2 data
340 to be of liquid-phase. We assume that clouds are weakly precipitating clouds if the cloud
341 liquid water path (LWP) $< 300 \text{ g m}^{-2}$. We require that the sensor and solar zenith angles
342 (θ) at that pixel are less than 30° and 60° , respectively. The maximum θ requirement is
343 motivated by the findings of Grosvenor and Wood (2014) who find that systematic errors
344 in MODIS retrievals increase significantly for $\theta > 60^\circ$. The θ requirement causes us to
345 focus on the months from November through February. We require at least 1000 1-km
346 resolution pixels with these characteristics to exist within a scene (typical number
347 > 10000). In addition, we require that no more than 10% of the pixels have a cloud top
348 temperature less than -20°C to ensure the absence of ice phase hydrometeors. Cloud
349 properties within a scene are averaged.

350

Formatted: Font: Italic

Formatted: Font: Italic, Subscript

351 Collocated cloud albedos (A) of the cloud scenes are analyzed. A is derived from the
352 Clouds and the Earth's Radiant Energy System (CERES) Energy Balanced and Filled
353 (EBAF) version 4.0 (Loeb et al, 2018) data collected using instruments on board Aqua
354 and Terra. The albedo is derived by dividing the upwelling shortwave flux at the top of
355 the atmosphere (TOA) by the downwelling shortwave flux at TOA. Because A has a
356 solar zenith angle dependence, (Minnis et al. 1998), we normalize all albedo values to
357 $\theta=45^\circ$ (approximately the mean value of θ for the analysis domain and months
358 analyzed) with an empirical method using theoretically calculated A (A) as a function of
359 latitude presented in Minnis et al. (1998 – their figure 7). The normalization is
360 implemented by first approximating the latitudinal dependence of A for various cloud
361 optical depths (τ) using the following regression equation: $A = 0.51 - 0.43\mu_0^{1/2} +$
362 $0.17\ln \tau$ where $\mu_0 = \cos \theta$. A approximates the variation of A with latitude within ~15%
363 at $\tau=8$. The fit decreases in accuracy at higher and lower τ increasing to an uncertainty
364 of ~30% for $\tau=2$ and $\tau=32$ (these values of τ (2, 8, 32) are those presented in Minnis et
365 al., 1998, Figure 7). The averaged τ of the MBL cloud scenes in our analysis is
366 approximately between 9 and 11 (Figure 5) so we expect that A is typically a reasonable
367 approximation of A . The normalization of all A to $\theta = 45^\circ$ is accomplished by
368 multiplying the CERES A by the ratio $\frac{A(\mu_0(\theta=45),\tau)}{A(\mu_0,\tau)}$ where τ is from the MODIS cloud
369 scene. The magnitude of the ratio applied to the data ranges from 0.85 at higher
370 latitudes to 1.2 at lower latitudes with an average near 1.

371
372 Author Contributions: GM led the overall conception, data analysis of the study and
373 interpretation of the results. SB was responsible for implementing data analysis code
374 and generation of figures. RH provided background on aerosol and provided insight
375 regarding various aspects of the study. MPG and ES assisted GM in the study design
376 and implementation.

377
378 Competing Interests: The authors declare no conflict of interest.

379
380 Acknowledgements: This work was supported by NASA Grant 80NSSC21k1969 and
381 DOE ASR Grants DE-SC00222001 and DE-SC0018995. All data used in this study are
382 available in public archives. Computer code for this study including all analysis code
383 and graphic generation code is written in the IDL language. Code is available upon
384 request to the corresponding author.

385
386 References

387
388 Arrigo, K. R., van Dijken, G. L., & Bushinsky, S. (2008). Primary production in the
389 Southern Ocean, 1997–2006. *Journal of Geophysical Research*, 113(C8).
390 <https://doi.org/10.1029/2007jc004551>
391 Behrenfeld, M. J., Hu, Y., O'Malley, R. T., Boss, E. S., Hostetler, C. A., Siegel, D. A.,
392 Sarmiento, J. L., Schulien, J., Hair, J. W., Lu, X., Rodier, S., & Scarino, A. J.
393 (2016). Annual boom–bust cycles of polar phytoplankton biomass revealed by
394 space-based Lidar. *Nature Geoscience*, 10(2), 118–122.
395 <https://doi.org/10.1038/ngeo2861>

396 Bodas-Salcedo, A., Hill, P. G., Furtado, K., Williams, K. D., Field, P. R., Manners, J. C.,
 397 Hyder, P., & Kato, S. (2016). Large contribution of supercooled liquid clouds to
 398 the solar radiation budget of the Southern Ocean. *Journal of Climate*, 29(11),
 399 4213–4228. <https://doi.org/10.1175/jcli-d-15-0564.1>

400 Brechtel, F. J., Kreidenweis, S. M., & Swan, H. B. (1998). Air mass characteristics,
 401 aerosol particle number concentrations, and number size distributions at
 402 Macquarie Island during the first aerosol characterization experiment (ACE 1).
 403 *Journal of Geophysical Research: Atmospheres*, 103(D13), 16351–16367.
 404 <https://doi.org/10.1029/97jd03014>

405 Carslaw, K. S., Lee, L. A., Reddington, C. L., Pringle, K. J., Rap, A., Forster, P. M.,
 406 Mann, G. W., Spracklen, D. V., Woodhouse, M. T., Regayre, L. A., & Pierce, J.
 407 R. (2013). Large contribution of natural aerosols to uncertainty in indirect forcing.
 408 *Nature*, 503(7474), 67–71. <https://doi.org/10.1038/nature12674>

409 Cavagna, A. J., Fripiat, F., Elskens, M., Mangion, P., Chirurgical, L., Closset, I.,
 410 Lasbleiz, M., Florez-Leiva, L., Cardinal, D., Leblanc, K., Fernandez, C., Lefèvre,
 411 D., Oriol, L., Blain, S., Quéguiner, B., & Dehairs, F. (2015). Production regime
 412 and associated n cycling in the vicinity of Kerguelen Island, Southern Ocean.
 413 *Biogeosciences*, 12(21), 6515–6528. <https://doi.org/10.5194/bg-12-6515-2015>

414 Deppeler, S. L., & Davidson, A. T. (2017). Southern Ocean Phytoplankton in a changing
 415 climate. *Frontiers in Marine Science*, 4. <https://doi.org/10.3389/fmars.2017.00040>

416 Fossum, K. N., Ovadnevaite, J., Ceburnis, D., Preißler, J., Snider, J. R., Huang, R.-J.,
 417 Zuend, A., & O'Dowd, C. (2020). Sea-spray regulates sulfate cloud droplet
 418 activation over oceans. *Npj Climate and Atmospheric Science*, 3(1).
 419 <https://doi.org/10.1038/s41612-020-0116-2>

420 Glassmeier, F., Hoffmann, F., Johnson, J. S., Yamaguchi, T., Carslaw, K. S., & Feingold, G. (2021).
 421 Aerosol-cloud-climate cooling overestimated by ship-track data. *Science*, 371(6528), 485-
 422 489.

423 Gras, J. L., & Keywood, M. (2017). Cloud condensation nuclei over the Southern
 424 Ocean: Wind dependence and seasonal cycles. *Atmospheric Chemistry and
 425 Physics*, 17(7), 4419–4432. <https://doi.org/10.5194/acp-17-4419-2017>

426 Grosvenor, D. P. and Wood, R.: The effect of solar zenith angle on MODIS cloud optical
 427 and microphysical retrievals within marine liquid water clouds, *Atmos. Chem.
 428 Phys.*, 14, 7291–7321, <https://doi.org/10.5194/acp-14-7291-2014>, 2014.

429 Grosvenor, D. P., Sourdeval, O., Zuidema, P., Ackerman, A., Alexandrov, M. D.,
 430 Bennartz, R., Boers, R., Cairns, B., Chiu, J. C., Christensen, M., Deneke, H.,
 431 Diamond, M., Feingold, G., Fridlind, A., Hünerbein, A., Knist, C., Kollias, P.,
 432 Marshak, A., McCoy, D., ... Quaas, J. (2018). Remote sensing of droplet number
 433 concentration in warm clouds: A review of the current state of knowledge and
 434 perspectives. *Reviews of Geophysics*, 56(2), 409–453.
 435 <https://doi.org/10.1029/2017rg000593>

436 Gryspeerd, E., Goren, T., Sourdeval, O., Quaas, J., Mülmenstädt, J., Dipu, S.,
 437 Unglaub, C., Gettelman, A., and Christensen, M.: Constraining the aerosol
 438 influence on cloud liquid water path, *Atmos. Chem. Phys.*, 19, 5331–5347,
 439 <https://doi.org/10.5194/acp-19-5331-2019>, 2019.

440 Hoppel, W. A., Frick, G. M., & Larson, R. E. (1986). Effect of nonprecipitating clouds on
441 the aerosol size distribution in the marine boundary layer. *Geophysical Research*
442 *Letters*, 13(2), 125–128. <https://doi.org/10.1029/gl013i002p00125>

443 Huang, Y., Siems, S. T., Manton, M. J., Rosenfeld, D., Marchand, R., McFarquhar, G.
444 M., & Protat, A. (2016). What is the role of sea surface temperature in modulating
445 cloud and precipitation properties over the Southern Ocean? *Journal of Climate*,
446 29(20), 7453–7476. <https://doi.org/10.1175/jcli-d-15-0768.1>

447 Humphries, R. S., Keywood, M. D., Gribben, S., McRobert, I. M., Ward, J. P., Selleck,
448 P., Taylor, S., Harnwell, J., Flynn, C., Kulkarni, G. R., Mace, G. G., Protat, A.,
449 Alexander, S. P., & McFarquhar, G. (2021). Southern Ocean latitudinal gradients
450 of cloud condensation nuclei. *Atmospheric Chemistry and Physics*, 21(16),
451 12757–12782. <https://doi.org/10.5194/acp-21-12757-2021>

452 Humphries, R. S., Klekociuk, A. R., Schofield, R., Keywood, M., Ward, J., & Wilson, S.
453 R. (2016). Unexpectedly high ultrafine aerosol concentrations above East
454 Antarctic Sea Ice. *Atmospheric Chemistry and Physics*, 16(4), 2185–2206.
455 <https://doi.org/10.5194/acp-16-2185-2016>

456 Kang, L., Marchand, R. T., Wood, R., & McCoy, I. L. (2022). Coalescence scavenging
457 drives droplet number concentration in Southern Ocean low clouds.
458 *Geophysical Research Letters*, 49, e2022GL097819.

459 Kanamitsu, M. (1989). Description of the NMC global data assimilation and forecast
460 system. *Weather and Forecasting*, 4(3), 335–342. [https://doi.org/10.1175/1520-0434\(1989\)004<0335:dotngd>2.0.co;2](https://doi.org/10.1175/1520-0434(1989)004<0335:dotngd>2.0.co;2)

462 Korhonen, H., Carslaw, K. S., Spracklen, D. V., Mann, G. W., & Woodhouse, M. T.
463 (2008). Influence of oceanic dimethyl sulfide emissions on cloud condensation
464 nuclei concentrations and seasonality over the remote Southern Hemisphere
465 oceans: A global model study. *Journal of Geophysical Research*, 113(D15).
466 <https://doi.org/10.1029/2007JD009718>

467 Krüger, O., & Graßl, H. (2011). Southern Ocean phytoplankton increases cloud albedo
468 and reduces precipitation. *Geophysical Research Letters*, 38(8).
469 <https://doi.org/10.1029/2011gl047116>

470 Lana, A., Simó, R., Vallina, S. M., & Dachs, J. (2012). Potential for a biogenic influence
471 on cloud microphysics over the ocean: A correlation study with satellite-derived
472 data. *Atmospheric Chemistry and Physics*, 12(17), 7977–7993.
473 <https://doi.org/10.5194/acp-12-7977-2012>

474 Latham, J., Rasch, P., Chen, C.-C., Kettles, L., Gadian, A., Gettelman, A., Morrison, H.,
475 Bower, K., & Choulaton, T. (2008). Global temperature stabilization via
476 controlled albedo enhancement of low-level maritime clouds. *Philosophical*
477 *Transactions of the Royal Society A: Mathematical, Physical and Engineering*
478 *Sciences*, 366(1882), 3969–3987. <https://doi.org/10.1098/rsta.2008.0137>

479 Mace, G. G. (2010). Cloud properties and radiative forcing over the maritime storm
480 tracks of the Southern Ocean and North Atlantic derived from A-train. *Journal of*
481 *Geophysical Research*, 115(D10). <https://doi.org/10.1029/2009jd012517>

482 Mace, G. G., & Avey, S. (2017). Seasonal variability of warm boundary layer cloud and
483 precipitation properties in the Southern Ocean as diagnosed from A-Train Data.
484 *Journal of Geophysical Research: Atmospheres*, 122(2), 1015–1032.
485 <https://doi.org/10.1002/2016jd025348>

486 Mace, G. G., Protat, A., & Benson, S. (2021). Mixed-phase clouds over the Southern
487 Ocean as observed from satellite and surface based Lidar and Radar. *Journal of*
488 *Geophysical Research: Atmospheres*, 126(16).
489 <https://doi.org/10.1029/2021jd034569>

490 Mace, G. G., Protat, A., Humphries, R. S., Alexander, S. P., McRobert, I. M., Ward, J.,
491 Selleck, P., Keywood, M., & McFarquhar, G. M. (2021). Southern ocean cloud
492 properties derived from Capricorn and Marcus Data. *Journal of Geophysical*
493 *Research: Atmospheres*, 126(4). <https://doi.org/10.1029/2020jd033368>

494 McCoy, D. T., Burrows, S. M., Wood, R., Grosvenor, D. P., Elliott, S. M., Ma, P.-L.,
495 Rasch, P. J., & Hartmann, D. L. (2015). Natural aerosols explain seasonal and
496 spatial patterns of Southern Ocean Cloud albedo. *Science Advances*, 1(6).
497 <https://doi.org/10.1126/sciadv.1500157>

498 McCoy, I. L., McCoy, D. T., Wood, R., Regayre, L., Watson-Parris, D., Grosvenor, D. P.,
499 Mulcahy, J. P., Hu, Y., Bender, F. A.-M., Field, P. R., Carslaw, K. S., & Gordon,
500 H. (2020). The hemispheric contrast in cloud microphysical properties constrains
501 aerosol forcing. *Proceedings of the National Academy of Sciences*, 117(32),
502 18998–19006. <https://doi.org/10.1073/pnas.1922502117>

503 McCoy, I. L., McCoy, D. T., Wood, R., Regayre, L., Watson-Parris, D., Grosvenor, D. P.,
504 Mulcahy, J. P., Hu, Y., Bender, F. A.-M., Field, P. R., Carslaw, K. S., & Gordon,
505 H. (2020). The hemispheric contrast in cloud microphysical properties constrains
506 aerosol forcing. *Proceedings of the National Academy of Sciences*, 117(32),
507 18998–19006. <https://doi.org/10.1073/pnas.1922502117>

508 McFarquhar, G. M., Bretherton, C. S., Marchand, R., Protat, A., DeMott, P. J.,
509 Alexander, S. P., Roberts, G. C., Twohy, C. H., Toohey, D., Siems, S., Huang,
510 Y., Wood, R., Rauber, R. M., Lasher-Trapp, S., Jensen, J., Stith, J. L., Mace, J.,
511 Um, J., Järvinen, E., ... McDonald, A. (2021). Observations of clouds, aerosols,
512 precipitation, and surface radiation over the Southern Ocean: An overview of
513 Capricorn, Marcus, MICRE, and socrates. *Bulletin of the American*
514 *Meteorological Society*, 102(4). <https://doi.org/10.1175/bams-d-20-0132.1>

515 Meskhidze, N., & Nenes, A. (2006). Phytoplankton and cloudiness in the Southern
516 Ocean. *Science*, 314(5804), 1419–1423.
517 <https://doi.org/10.1126/science.1131779>

518 Miller, M. A., & Yuter, S. E. (2008). Lack of correlation between chlorophylla and cloud
519 droplet effective radius in shallow marine clouds. *Geophysical Research Letters*,
520 35(13). <https://doi.org/10.1029/2008gl034354>

521 Minnis, P., D. P. Garber, D. F. Young, R. F. Arduini, Y. Takano, 1998:
522 Parameterizations of reflectance and effective emittance for satellite remote
523 sensing of cloud properties. *Journal of the Atmospheric Sciences*, 55, 3313-
524 3339.

525 MODIS Characterization Support Team (MCST), 2017. MODIS Geolocation Fields
526 Product. NASA MODIS Adaptive Processing System, Goddard Space Flight
527 Center, USA: <http://dx.doi.org/10.5067/MODIS/MOD03.061>

528 NASA. (n.d.). *Modis/terra clouds 5-min L2 Swath 1km and 5km - LAADS DAAC*. NASA.
529 Retrieved March 2, 2022, from
530 [https://ladsweb.modaps.eosdis.nasa.gov/missions-and-](https://ladsweb.modaps.eosdis.nasa.gov/missions-and-measurements/products/MOD06_L2)
531 [measurements/products/MOD06_L2](https://ladsweb.modaps.eosdis.nasa.gov/missions-and-measurements/products/MOD06_L2)

532 Naud, C. M., Booth, J. F., & Del Genio, A. D. (2016). The relationship between
533 boundary layer stability and cloud cover in the post-cold-frontal region. *Journal of*
534 *Climate*, 29(22), 8129–8149. <https://doi.org/10.1175/jcli-d-15-0700.1>

535 [Painemal, D., J.-Y. C. Chiu, P. Minnis, C. Yost, X. Zhou, M. Cadeddu, E. Eloranta, E. R.](#)
536 [Lewis, R. Ferrare, and P. Kollias \(2017\), Aerosol and cloud microphysics covariability in](#)
537 [the northeast Pacific boundary layer estimated with ship-based and satellite remote](#)
538 [sensing observations. *J. Geophys. Res. Atmos.*, 122, doi:10.1002/2016JD025771,](#)
539 Platnick, S., Ackerman, S., King, M., et al., 2015. MODIS Atmosphere L2 Cloud Product
540 (06_L2). NASA MODIS Adaptive Processing System, Goddard Space Flight Center,
541 USA: http://dx.doi.org/10.5067/MODIS/MOD06_L2.061

542 Shaw, G. E. (2007). Do biologically produced aerosols really modulate climate?
543 *Environ. Chem.* 4, 382–383, doi:10.1071/EN07073.

544 Shaw, G. E. (1988). Antarctic Aerosols: A Review. *Reviews of Geophysics*, 26(1), 89–
545 112.

546 Stein, A. F., Draxler, R. R., Rolph, G. D., Stunder, B. J., Cohen, M. D., & Ngan, F.
547 (2015). NOAA's Hysplit Atmospheric Transport and dispersion modeling system.
548 *Bulletin of the American Meteorological Society*, 96(12), 2059–2077.
549 <https://doi.org/10.1175/bams-d-14-00110.1>

550 Stein, A. F., Draxler, R. R., Rolph, G. D., Stunder, B. J., Cohen, M. D., & Ngan, F.
551 (2015). NOAA's Hysplit Atmospheric Transport and dispersion modeling system.
552 *Bulletin of the American Meteorological Society*, 96(12), 2059–2077.
553 <https://doi.org/10.1175/bams-d-14-00110.1>

554 Stephens, G. L., 1978: Radiation profiles in extended water clouds. II: Parameterization
555 schemes. *J. Atmos. Sci.*, 35, 2123–2132, [https://doi.org/10.1175/1520-0469\(1978\)035<2123:RPIEWC.2.0.CO;2](https://doi.org/10.1175/1520-0469(1978)035<2123:RPIEWC.2.0.CO;2).

556

557 Trenberth, K. E., & Fasullo, J. T. (2010). Simulation of present-day and twenty-first-
558 century energy budgets of the Southern Oceans. *Journal of Climate*, 23(2), 440–
559 454. <https://doi.org/10.1175/2009jcli3152.1>

560 Twohy, C. H., & Anderson, J. R. (2008). Droplet nuclei in non-precipitating clouds:
561 Composition and Size matter. *Environmental Research Letters*, 3(4), 045002.
562 <https://doi.org/10.1088/1748-9326/3/4/045002>

563 Twohy, C. H., DeMott, P. J., Russell, L. M., Toohey, D. W., Rainwater, B., Geiss, R.,
564 Sanchez, K. J., Lewis, S., Roberts, G. C., Humphries, R. S., McCluskey, C. S.,
565 Moore, K. A., Selleck, P. W., Keywood, M. D., Ward, J. P., & McRobert, I. M.
566 (2021). Cloud-nucleating particles over the Southern Ocean in a changing
567 climate. *Earth's Future*, 9(3). <https://doi.org/10.1029/2020ef001673>

568 Vallina, S. M., Simó, R., & Gassó, S. (2006). What controls CCN seasonality in the
569 Southern Ocean? A statistical analysis based on satellite-derived chlorophyll and
570 CCN and model-estimated oh radical and rainfall. *Global Biogeochemical Cycles*,
571 20(1). <https://doi.org/10.1029/2005gb002597>

572 Woodhouse, M. T., Mann, G. W., Carslaw, K. S., & Boucher, O. (2013). Sensitivity of
573 cloud condensation nuclei to regional changes in dimethyl-sulphide emissions.
574 *Atmospheric Chemistry and Physics*, 13(5), 2723–2733.
575 <https://doi.org/10.5194/acp-13-2723-2013>

576

577

Deleted: ¶

Formatted: Font: (Default) Arial, 12 pt, Not Italic

Deleted: Petters, M. D., & Kreidenweis, S. M. (2007). A single parameter representation of hygroscopic growth and cloud condensation nucleus activity. *Atmospheric Chemistry and Physics*, 7(8), 1961–1971. <https://doi.org/10.5194/acp-7-1961-2007> ¶

Formatted: Indent: Left: 0", First line: 0"